Sensing Sea Ice Based on Doppler Spread Analysis of Spaceborne GNSS-R Data

Yongchao Zhu, Tingye Tao, Kegen Yu, *Senior Member, IEEE*, Zhenxuan Li, Xiaochuan Qu, Zhourun Ye, Jun Geng, Jingui Zou, Maximilian Semmling, and Jens Wickert

***Abstract*—The spaceborne Global Navigation Satellite System-Reflectometry (GNSS-R) delay-Doppler map (DDM) data collected over ocean carry typical feature information about the ocean surface, which may be covered by open water, mixed water/ice, complete ice, etc. A new method based on Doppler spread analysis is proposed to remotely sense sea ice using the spaceborne GNSS-R data collected over the Northern and Southern Hemispheres. In order to extract useful information from DDM, three delay waveforms are defined and utilized. The delay waveform without Doppler shift is defined as central delay waveform (CDW), while the integration of delay waveforms of 20 different Doppler shift values is defined as integrated delay waveform (IDW). The differential waveform between normalized CDW (NCDW) and normalized IDW (NIDW) is defined as differential delay waveform (DDW), which is a new observable used to describe the difference between NCDW and NIDW, which have different Doppler spread characteristics. The difference is mainly caused by the roughness of reflected surface. First, a new data quality control method is proposed based on the standard deviation and root-mean-square error (RMSE) of the first 48 bins of DDW. Then, several different observables derived from NCDW, NIDW, and DDW are applied to distinguish sea ice from water based on their probability density function. Through validating against sea ice edge data from the Ocean and Sea Ice Satellite Application Facility, the trailing edge waveform summation of DDW achieves the best results, and its probabilities of successful detection are 98.22% and 96.65%, respectively, in the Northern and Southern Hemispheres.**

***Index Terms*—Central delay waveform (CDW), delay-Doppler map (DDM), differential delay waveform (DDW), Global Navigation Satellite System-Reflectometry (GNSS-R), integrated delay waveform (IDW), sea ice sensing.**

Manuscript received June 11, 2019; revised September 19, 2019; accepted November 19, 2019. Date of publication December 12, 2019; date of current version February 12, 2020. This work was supported in part by the Fundamental Research Funds for the Central Universities of China under Grant JZ2019HGBZ0139, in part by the National Natural Science Foundation of China under Grant 41871313, and in part by the Natural Science Foundation of Anhui Province, China, under Grant 1808085MD105. *(Corresponding author: Yongchao Zhu.)*

Y. Zhu, T. Tao, Z. Li, X. Qu, Z. Ye, and J. Geng are with the College of Civil Engineering, Hefei University of Technology, Hefei 230009, China (e-mail: yczhu@hfut.edu.cn; czytty@163.com; zxlicumt@126.com; qqxxcc@hotmail.com; yezhourun329@hotmail.com; gaoyugengjun@163.com).

K. Yu is with the School of Environment Science and Spatial Informatics, China University of Mining and Technology, Xuzhou 221116, China (e-mail: kegen.yu@foxmail.com).

J. Zou is with the School of Geodesy and Geomatics, Wuhan University, Wuhan 430079, China (e-mail: jgzou@sgg.whu.edu.cn).

M. Semmling and J. Wickert are with the German Research Center for Geosciences GFZ, Potsdam 14473, Germany (e-mail: maxsem@gfz-potsdam.de; wickert@gfz-potsdam.de).

Digital Object Identifier 10.1109/JSTARS.2019.2955175

I. Introduction

THE CRYOSPHERE has been studied for a long time and it is still being highly focused. As one of the most important elements of the cryosphere, sea ice coverage is a crucial parameter that affects the global climate and maritime industry [1]. Moreover, a lot of people are living in the polar region, therefore having a good knowledge of sea ice information benefits a lot for their living [2]. Sea ice was mainly found in remote polar oceans and it can be observed using remote sensing techniques, which are currently considered as the most efficient and effective way to monitor sea ice [3]. Global Navigation Satellite System Reflectometry (GNSS-R) is an innovative remote sensing technology that exploits signals transmitted from GNSS satellites and scattered off the Earth surface. GNSS-R for remote sensing applications was first discussed in 1988 [4]. The application for ocean altimetry of GNSS-R was initially presented by Martin-Neira [5]. The capability of GNSS-R for ocean remote sensing has been expanded significantly over the past decades [6]. Applications to ocean are mostly focused on sea surface over open water, such as ocean wind retrieval [7], [8], ocean tides detection [9], tsunami detection and parameter estimation [10], [11], target detection [12], and sea surface altimetry [13]. Besides, GNSS-R has shown great potential for land remote sensing, such as soil moisture demonstration [14], vegetation observation [15], and snow depth measurement [16]. This article focuses on exploiting the sea ice sensing capability of GNSS-R.

The idea of using GNSS-R for sea ice detection was first demonstrated by Komjathy *et al.* [17] through comparing the waveform peak power of GNSS signals over ice against RADARSAT backscattering echoes. In 2003, Wiehl *et al.* [18] proposed a theoretical model for illustrating the scattering mechanism of ice sheet. Then, the permittivity and roughness of different kinds of sea ice were studied by analyzing the shape of reflected signals' waveforms [19]. Spaceborne GNSS-R for sea ice detection was initially presented by Gleason [20] and more details were demonstrated in 2010 [21] using GNSS-R dataset from the United Kingdom-Disaster Monitoring Constellation (UK-DMC) launched in 2003. Ground-based GNSS-R for sea ice altimetry was evaluated in [22] based on the coherent differential phase between direct and both cross- and co-polar reflected signals. Two other sea ice detection methods using ground-based GNSS-R were presented in [23]. Later, sea ice concentration determination based on ground-based GNSS-R was

performed using data collected in Bohai Bay sea ice experiment [24]. The successful launch of the TechDemoSat-1 (TDS-1) in 2014 created opportunities of spaceborne GNSS-R for sea ice study as a large number of datasets collected over the Arctic and Antarctic region are available online (www.merrbys.co.uk) [25]. Spaceborne GNSS-R for sea ice altimetry studies was demonstrated in three latest papers [26]–[28]. Sea ice detection using TDS-1 data was initially presented through calculating the pixel number of each DDM by Yan *et al.* [29], followed by their investigation of sea ice concentration retrieval using the neural networks technique [30], [31]. Another sea ice detection method was studied in [32] through estimating the similarity of received reflected waveform and theoretical waveform, which is promising in the sea ice determination, but not very effective for ice concentration retrieval. Two effective sea ice detection algorithms based on differential DDMs were illustrated in [33], which uses a new GNSS-R observable to distinguish sea ice from water.

In this article, the potential of GNSS-R for sea ice sensing is studied through analyzing observables obtained based on the Doppler spread analysis. Section II presents the theory and mathematical model, which is the basis of the proposed sea ice sensing approach. Section III describes the characteristics of TDS-1 dataset and data preprocessing scheme. Several GNSS-R observables derived from the TDS-1 data are also presented. Section IV shows the GNSS-R sea ice sensing results and the proposed GNSS-R approaches are evaluated against available sea ice data obtained using microwave remote sensing sensors. Finally, Section V concludes this article.

II. Theory and Mathematical Model

Spaceborne GNSS-R can be regarded as a bistatic radar-scatterometer. In order to illustrate the power of scattered GNSS signals, a theoretical integrated delay waveform (IDW) model that describes the power of scattered signals as a function of time delay was proposed in [34]

$$W_I(\tau) = T_i^2 \int \frac{D^2(\vec{\rho})}{4\pi R_T^2(\vec{\rho}) R_R^2(\vec{\rho})} |\chi(\tau,\ f_D(\vec{\rho}))|^2 \sigma_0(\vec{\rho})\, d^2\rho \tag{1}$$

where τ is the time delay value, T_i is the coherent integration time, R_T is the distance from the GNSS transmitter to the scattering point, R_R is the distance from the scattering point to the receiver, D^2 is the function of power antenna footprint, f_D is the Doppler shift frequency, ρ is a vector from the specular reflection point to the scattering point, and χ stands for the Woodward's ambiguity function (WAF) [35]

$$\chi(\tau, f_D) = \Lambda(\tau - (R_T(\vec{\rho}) + R_R(\vec{\rho}))/c) \times S(f_D(\vec{\rho}) - f_c) \tag{2}$$

where c and f_c are, respectively, the propagation velocity and frequency of electromagnetic wave; χ is approximated by a triangular function Λ in the time domain and by a sinc function S in the frequency domain; and σ_0 is the normalized bistatic radar cross section

$$\sigma_0(\vec{\rho}) = \frac{\pi |\Re(\vec{\rho})|^2 q^4(\vec{\rho})}{q_z^4(\vec{\rho})} P\left(-\frac{q_\perp(\vec{\rho})}{q_z(\vec{\rho})}\right) \tag{3}$$

where $\Re$ is the Fresnel reflection coefficient, q is the scattering vector, q_z is the vertical component of the scattering vector, $q_\perp$ stands for the x and y components of the scattering vector, and $P(\vec{S})$ is the probability density function (PDF) of slopes.

Now, we can define the positive (Δf_+) and negative (Δf_-) Doppler spreading as follows:

$$\begin{cases} \Delta f_+ = f_{\max} - f_{\mathrm{SP}} \\ \Delta f_- = f_{\mathrm{SP}} - f_{\min} \end{cases} \tag{4}$$

where f_{SP} is the Doppler shift of radio wave reflected from the specular point, and $f_{\max}$ and $f_{\min}$ are, respectively, the maximum and minimum Doppler shift of the scattered signal.

The coherent integration time can be set to be 1 ms and the Doppler bandwidth $\Delta f_0 = 1/2T_i$. According to the analysis in [41], the Doppler effects can be neglected when the width of the glistening zone is smaller than the Doppler bandwidth (i.e., $\Delta f_+ + \Delta f_- < \Delta f_0$). Then, the sinc function $S(f_D(\vec{\rho}) - f_c)$ is equal to 1 and the central delay waveform (CDW) without Doppler shift can be obtained based on (1) and (2) as

$$W_C(\tau) = T_i^2 \int \frac{D^2(\vec{\rho})}{4\pi R_T^2(\vec{\rho}) R_R^2(\vec{\rho})} |\Lambda|^2 \sigma_0(\vec{\rho})\, d^2\rho. \tag{5}$$

The difference between CDW and IDW for sea ice is smaller than that for sea water because the scattered signal usually shows a diffusive and incoherent nature over the open water. That is, the difference significantly depends on sea surface conditions. The differential delay waveform (DDW) between normalized IDW (NIDW) and normalized CDW (NCDW) can be described by

$$W_D(\tau) = W_I^N(\tau) - W_C^N(\tau) \tag{6}$$

where τ is the delay value, *D* represents the differential delay waveform (DDW), $W_D(\tau)$ stands for the DDW, *N* represents the normalization of delay waveforms, and $W_I^N(\tau)$ and $W_C^N(\tau)$ represent NIDW and NCDW, respectively.

III. Dataset Description and Data Processing

A. Spaceborne GNSS-R DDM and Delay Waveforms

The Space GNSS Receiver Remote Sensing Instrument (SGR-ReSI) [36] onboard TDS-1 receives signals scattered off the Earth and generates DDMs through cross correlating collected scattered signals with locally generated code replicas for different time delays and Doppler shifts [36]. TDS-1 data downloaded from the Measurement of Earth Reflected Radionavigation Signals by Satellite (MERRByS) are the dataset used in this article. The standard GNSS-R DDMs employ 1000-ms incoherent integration in order to mitigate the effect of noise floor. The shapes of measured DDMs are influenced by the characteristics of the surface where the signals are scattered off. The delay waveforms are used as basic observables in this article

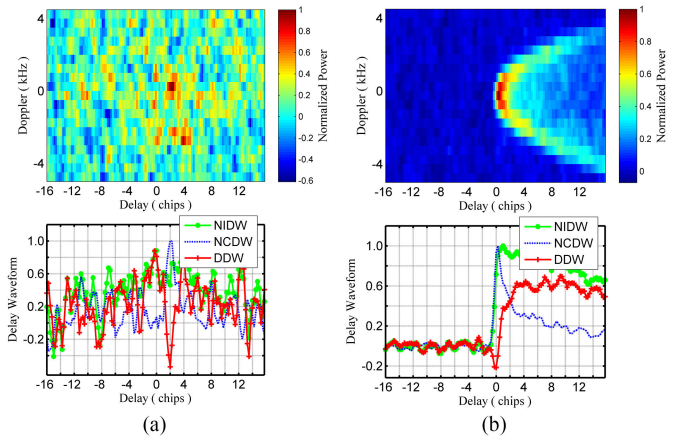

Fig. 1. Normalized DDM and corresponding delay waveforms with (a) low SNR (SNR = 0.1927 dB) and (b) large SNR (SNR = 1.5009 dB) collected over the ocean. NIDW is the normalization of integrated delay waveform (NIDW). NCDW is the normalization of central delay waveform with zero delay. DDW is the differential delay waveform between NIDW and NCDW.

for sensing sea ice. In order to focus on effects caused by the surface reflection, only a part of delay bins is picked out as several starting delay bins are dominated by noise and several ending delay bins are severely affected by reflections over areas far away from the specular point.

Data preprocessing is conducted using the methods described in [33]. As illustrated in [33], the peak signal-to-noise ratio (SNR) of DDM is usually used as an indicator to filter low-quality data which cannot be used for extracting effective GNSS-R observables. However, the peak SNR can only represent the quality of the DDM associated with one point which is usually the specular point, not the whole DDM. A new statistical data filtering scheme is proposed here with details described as follows. As mentioned in Section II, NCDW, NIDW, and DDW are extracted from normalized DDMs. Two typical DDMs and corresponding delay waveforms with different situations are shown in Fig. 1, using data collected on 29 February, 2016 over the ocean.

As shown in Fig. 1, the values of DDW with low SNR (large noise) show distinctive difference and larger dispersion over the starting several delay bins, while reverse for DDW with large SNR (small noise). The large noise may be caused by the space environment for signal propagation, such as atmospheric attenuation, spatial signal interference, and propagation loss. The data quality is also affected by the incidence angle, antenna gain, and satellite attitude. The standard deviation (SD) describes the degree of dispersion of a set of data, which is defined as

$$\mathrm{SD}_n = \sqrt{\sum_{i=1}^{n} \left(W_i^D - \bar{W}\right)^2 \Big/ n} \tag{7}$$

where W_i^D is the ith sample value of the DDW, and $\bar{W}$ is the mean of n sample values.

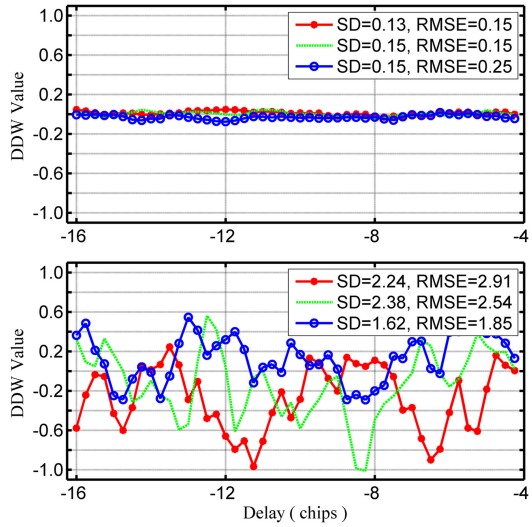

Fig. 2. SD and RMSE of the starting 48 delay bins of DDW with (upper) large SNR and (lower) small SNR for three different situations.

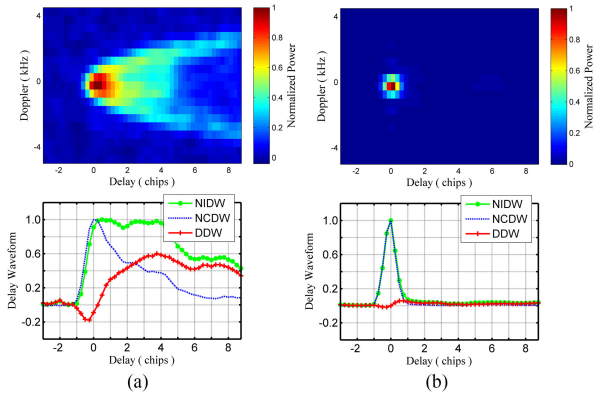

Fig. 3. Processed TDS-1 DDMs and corresponding delay waveforms over (a) sea water and (b) sea ice.

The root-mean-square error (RMSE) represents the difference between measured values and true values

$$\mathrm{RMSE}_n = \sqrt{\sum_{i=1}^{n} \left(W_i^D - \hat{W}\right)^2 \Big/ n} \tag{8}$$

where $\hat{W}$ is the most probable value of DDW. The DDW data over the first 48 delay bins (12 C/A code chips) are adopted in this article for data filtering.

The DDW distribution over the first 48 delay bins (12 C/A code chips from chips -16 to -4) with different qualities is presented in Fig. 2. The data in Figs. 1 and 2 are not exactly the same. Fig. 1 presents just one sample of large noise (left) and small noise (right), whereas Fig. 2 shows another three samples of large noise (lower) and small noise (upper). The data with SD above 0.3 and RMSE above 0.5 are excluded in this article as they are contaminated by noise.

After data preprocessing, the processed DDMs and corresponding delay waveforms collected over sea water and ice are presented in Fig. 3, using data collected on 29 Feb. 2016 over the Northern Hemisphere (NH).

The normalized integral of the DDMs over the Doppler domain (NIDW) describes the power spreading due to roughness over the delay domain. As shown in Fig. 3, the spreading of DDM over sea water shows "horseshoe" shape and the corresponding NIDW and NCDW show different characteristics, which can be expressed by DDW. On the other hand, there is less spreading of DDM over sea ice, whose NIDW and NCDW show less spreading too. These features provide opportunities to distinguish sea ice from water.

B. GNSS-R Observables

Several observables associated with DDM have been proposed for different GNSS-R applications in some previous studies. Some heuristic observables, such as the leading edge slope, trailing edge slope (TES), DDM average (DDMA), DDM variance (DDMV), and Allan DDMV (ADDMV) were used to retrieve wind speed in [37]. The characteristics of these forward observables were studied in [32] using TDS-1 data, produced with 1-s incoherent integration of 1-ms coherently integrated DDMs. Only DDMs with 1-s incoherent summation are available to us, and therefore observables, such as DDMV and ADDMV, obtained based on 1-ms coherently integrated DDM cannot be used. For illustration purposes, the delay waveform can be divided into leading edge and trailing edge from the point with zero time delay of NCDW. As shown in Fig. 3, the leading edge of delay waveforms of sea ice and water shows less difference as the leading edge is almost not affected by the surface roughness. TES is an important observable used for retrieving geophysical parameters, such as wind speed. Particularly, the TES of NIDW is used to distinguish sea ice from water and the results of TES algorithm show great potential for sea ice detection [32]. Another classical observable termed as DDMA is used in [32] to detect sea ice and its performance is a little worse than that of TES. The literature [32] also analyzed some other heuristic observables and proposed a matched filter (MF) approach, whose performance is similar to that of NIDW TES algorithm.

As introduced above, three delay waveforms termed as NCDW, NIDW, and DDW are used as basic observables in this article. TES of these three delay waveforms is used as an indicator for sea ice sensing. The trailing edge waveform summation (TEWS) of delay waveforms is another observable used first in this article. The below is the definition of used GNSS-R observables.

1) TES: It is the slope of the trailing edge of delay waveforms. TES is computed through the least-squares fitting as

$$\mathrm{TES}_n = \left(\sum_{i=1}^{n} \tau_i W_i^T - n\bar{\tau}\overline{W^T}\right) \Bigg/ \left(\sum_{i=1}^{n} \tau_i^2 - n\bar{\tau}^2\right) \tag{9}$$

where n ($n \geq 2$) is the number of delay bins used for curve fitting; T_i is the time delay value of each point; W_i^T is the waveform value of trailing edge; $\bar{\tau}$ and $\overline{W^T}$ are the mean of time delay and waveform values of points applied for fitting, respectively. TES^C and TES^I are the slope of NCDW and NIDW, respectively; and TES^D is the slope of DDW. TES changes with the number of delay bins selected, therefore three different numbers of delay bins ($n = 3$, 5, and 7) are selected.

a) TES_3: 0.75 chips, the length of time delay is about 750 ns;
b) TES_5: 1.25 chips, the length of time delay is about 1.25 μs;
c) TES_7: 1.75 chips, the length of time delay is about 1.75 μs.

2) TEWS: It is the power summation of the trailing edge of delay waveforms, simply defined as

$$\mathrm{TEWS}_n = \sum_{i=1}^{n} W_i^T \tag{10}$$

where n delay bins are used for computing the TEWS; W_i is the waveform value of each point; TEWS^C and TEWS^I are the TEWS of NCDW and NIDW, respectively; and TEWS^D is the TEWS of DDW, which is equal to the difference between TEWS^C and TEWS^I as follows:

$$\mathrm{TEWS}^D = \mathrm{TEWS}^I - \mathrm{TEWS}^C. \tag{11}$$

It was observed from the analysis of DDW that the waveform shows variation from the fourth delay bin and it tends to be stable after 20 delay bins. Three different lengths of delay bins have been selected for computing TEWS:

a) TEWS_7: 1.75 chips, the length of time delay is about 1.75 μs;
b) TEWS_9: 2.25 chips, the length of time delay is about 2.25 μs;
c) TEWS_{11}: 2.75 chips, the length of time delay is about 2.75 μs.

C. Validation Dataset

The sea ice data from the Ocean and Sea Ice Satellite Application Facility (OSISAF) is used as the ground-truth data in this article. Sea ice datasets from the OSISAF are generated based on multichannel data of the Special Sensor Microwave Imager/Sounder (SSMIS) and ASCAT backscatter values, using a Bayesian approach [38]. The OSISAF data used in this article include sea ice edge (SIE) and sea ice type (SIT) data. The OSISAF data are provided with a resolution of 10 km and mapped in the polar stereographic projection [39]. More details about sea ice data from the OSISAF are presented in [39] and [40].

IV. Sea Ice Sensing Experiments

A. Experiment

In order to assess the applicability and reliability of the proposed methods, all available TDS-1 data with a latitude larger than 31° for the NH and lower than −39° for the Southern Hemisphere (SH) from January 2015 to April 2016 are used in this article. There are 46 periods of data, whose receiver data identifier (RD) is from RD16 to RD70 and some of them are missing maybe because of holidays, such as RD21, RD28–32, RD42, and RD57–RD58. As described in Section III, normalized delay

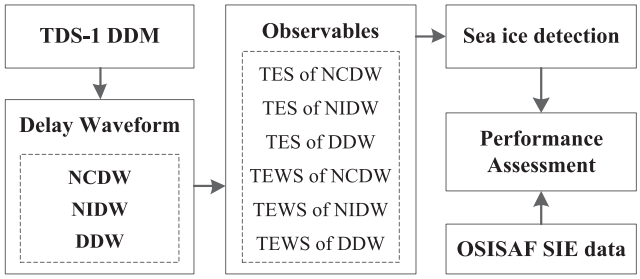

Fig. 4. Flow diagram of sea ice detection. Three delay waveforms (NCDW, NIDW, and DDW) are first extracted from TDS-1 DDM. Hereafter, the TES and TEWS of three delay waveforms are used as GNSS-R observables to distinguish sea ice from water. Finally, the sea ice detection results are validated with the OSISAF SIE data.

waveforms are obtained based on several data preprocessing steps, which have been applied to TDS-1 data used in this article.

The TES and TEWS of three delay waveforms (NCDW, NIDW, and DDW) are used as decision variables for distinguishing sea ice from water. The flow chart of sea ice detection is shown in Fig. 4.

B. Results and Performance Evaluation

The PDFs of the three proposed decision variables were computed and several indicators have been used as the performance index. The plots of TES observables and TEWS observables have similar shapes. The TES and TEWS parameters with different delay bins show different sensitivity to sea ice sensing. Due to the limitation of layout size, one of each type of observables (TES and TEWS) was picked out to present according to their performance. The PDFs of the TES with 1.25 chips of the three algorithms for the NH and SH are shown in Fig. 5. The OSISAF SIE data are used as the ground truth as mentioned earlier. As shown in Fig. 5(a)–(c), the performance of the TES algorithm for the NH changes with the delay waveforms selected. The performance of TES_5^I is the best among the three different schemes. The performance of the TES algorithm for the SH of three different delay waveforms is shown in Fig. 5(d)– (f). It can be seen that the PDFs of the decision variables for the SH look similar to those for the NH. In general, the performance of TES^I is better than that of TES^C and TES^D. Moreover, it is clear that the detected sea ice values appear on the right-hand side, which is greater than the threshold for the TES^C and TES^I, whereas they appear on the left-hand side, which is smaller than the threshold for the TES^D.

Similarly, the PDFs of the TEWS with 1.75 chips for the NH and SH are shown in Fig. 6. Clearly, the performance of TEWS^C is the worst among the three schemes.

In order to assess the performance of the proposed approaches, several evaluation indicators are defined according to the PDF of the decision variables. Taking Fig. 5(f) as an example, the horizontal coordinate value corresponding to the intersection of the PDF of sea ice and water is the threshold, which is marked with green line. The integral of the PDF of sea ice on the left-hand side of the intersection is defined as the probability of ice detection (PID). The integral of the PDF of sea water on the

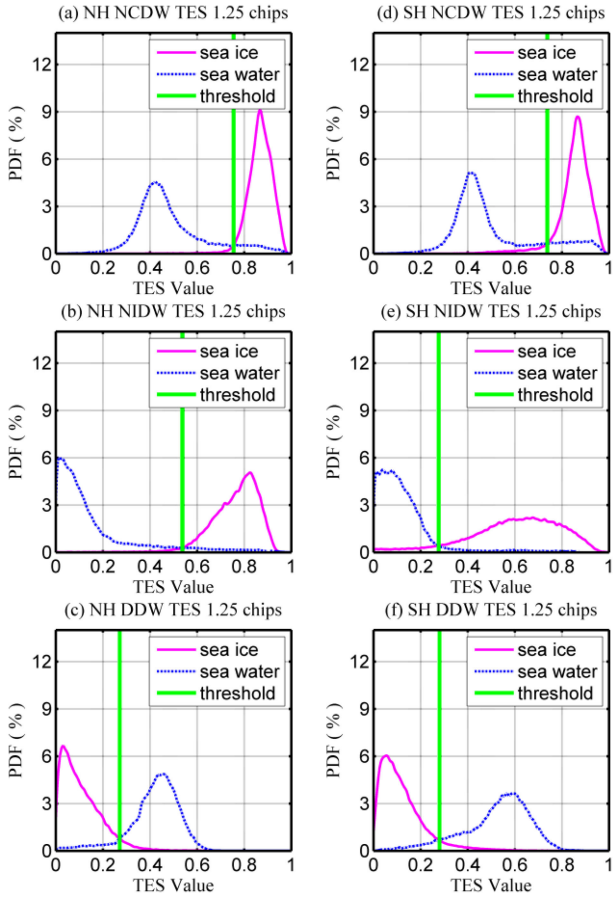

Fig. 5. TES 1.25 chips decision variables' performance for the Northern Hemisphere (NH) and Southern Hemisphere (SH) compared with the OSISAF SIE data. (a) NH TES_5^C. (b) NH TES_5^I. (c) NH TES_5^D. (d) SH TES_5^C. (e) SH TES_5^I. (f) SH TES_5^D.

right-hand side of the intersection is defined as the probability of water detection (PWD). The area of the region covered by the PDF of sea water on the left-hand side of the intersection is defined as the probability of false alarm for ice detection (PFAi) and is given as

$$\mathrm{PFAi} = 1 - \mathrm{PWD}. \tag{12}$$

Similarly, the area of the region covered by the PDF of sea ice on the right-hand side of the intersection is defined as the probability of false alarm for water detection (PFAw) and is given as

$$\mathrm{PFAw} = 1 - \mathrm{PID}. \tag{13}$$

Therefore, the overall evaluation indicator of sea ice sensing should be computed by PFAi and PFAw. That is, the probability of overall false detection (POF) is defined as

$$\mathrm{POF} = (\mathrm{PFAi} + \mathrm{PFAw})/2. \tag{14}$$

The probability of overall detection (POD) is equal to 100%-POF. Given the POF, the POD is known.

As introduced in Section III, there are three different delay bins selected for every observable. For illustration, the POF of

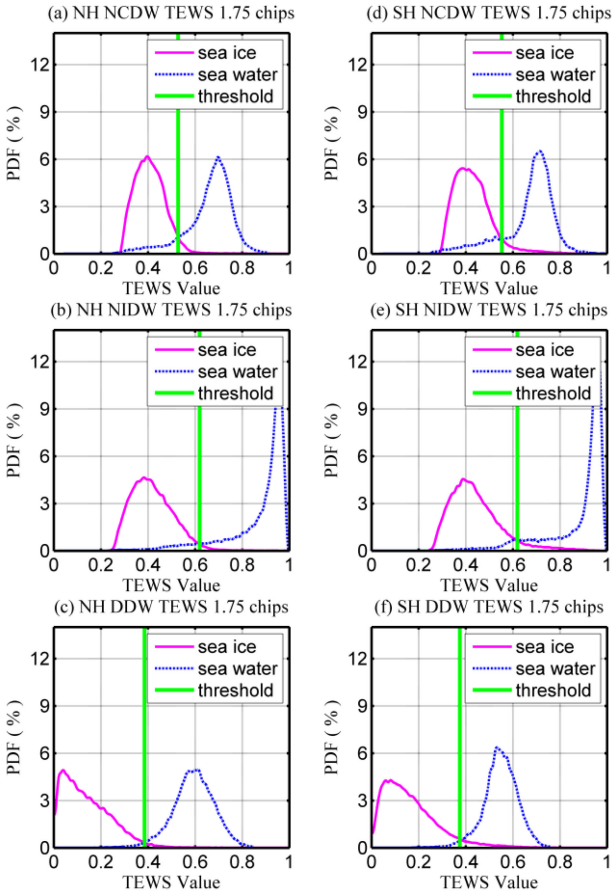

Fig. 6. TEWS 1.75 chips decision variables' performance for the Northern Hemisphere (NH) and Southern Hemisphere (SH) compared with the OSISAF SIE data. (a) NH TEWS_7^C. (b) NH TEWS_7^I. (c) NH TEWS_7^D. (d) SH TEWS_7^C. (e) SH TEWS_7^I. (f) SH TEWS_7^D.

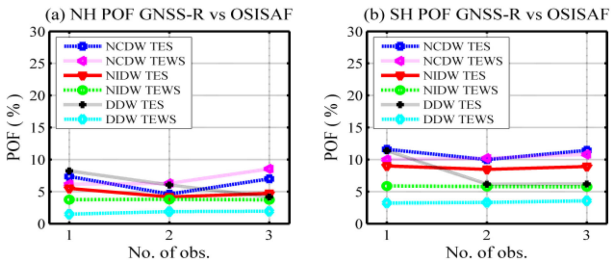

Fig. 7. Probability of overall false detection (POF) of proposed approaches with three different delay bins selected for the (a) Northern Hemisphere (NH) and (b) Southern Hemisphere (SH).

the proposed estimators with three different delay bins selected for the NH and SH is shown in Fig. 7.

In general, the performance of TEWS^D is better than that of others. The TEWS_7^D-based method achieves the best performance with a POF of 1.52%. For quantitative analysis, the overall performance of sea ice sensing is evaluated by the average performance of decision variables with three different delay bins selected. In addition, the MF [32] and pixel number of differential DDM (PN-D) [33] methods are further studied to obtain a thorough assessment of the performance of the proposed method. The MF and PN-D methods achieve a relatively good

TABLE I
Sea Ice Sensing Results of Proposed Approaches Compared With the OSISAF SIE Data for the Northern Hemisphere (NH) and Southern Hemisphere (SH)

		PID (%)	PWD (%)	PFAi (%)	PFAw (%)	POF (%)
NH	TES^C	98.55	88.83	11.17	1.45	6.31
	TES^I	98.25	92.17	7.83	1.75	4.79
	TES^D	95.66	92.06	7.94	4.34	6.14
	$TEWS^C$	97.07	88.96	11.04	2.93	6.98
	$TEWS^I$	98.74	93.78	6.22	1.26	3.74
	$TEWS^D$	97.56	98.87	1.13	2.44	1.78
	MF	97.17	96.22	3.78	2.83	3.31
	PN-D	97.12	96.33	3.67	2.88	3.28
SH	TES^C	95.97	82.02	17.98	4.03	11.00
	TES^I	94.19	88.24	11.76	5.81	8.78
	TES^D	93.15	91.09	8.91	6.85	7.88
	$TEWS^C$	94.44	84.91	15.09	5.56	10.33
	$TEWS^I$	93.84	94.55	5.45	6.16	5.80
	$TEWS^D$	95.22	98.08	1.92	4.78	3.35
	MF	95.01	96.11	3.89	4.99	4.44
	PN-D	95.18	96.14	3.86	4.82	4.34

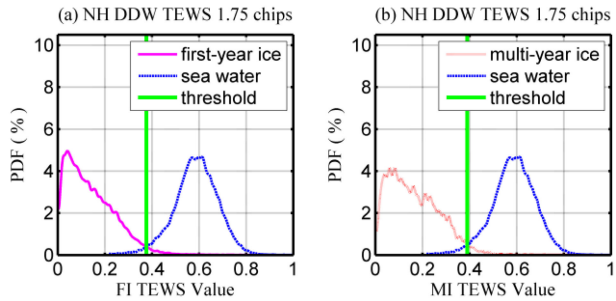

Fig. 8. Probability density function (PDF) of (a) first-year and (b) multiyear ice for the TEWS^D 1.75 chips decision variable.

performance with a POF of 3.31% and 3.28%, respectively, for the NH. The performance of MF is better than that of TES^I, while a little worse than that of TEWS^D. The overall sea ice sensing results obtained with the proposed approaches are presented in Table I. The PID and PWD of TEWS^D for the NH are larger than 97% and the average POF for three delay bins selected is 1.78%, which means the probability of successful detection is up to 98.22%. Regarding TEWS^C, although its PID is up to 97%, the PWD is lower than 90%; therefore, its POF is higher than that of others. It is worth noting that the POF of TEWS^D for the SH is about 1.57% larger than that for the NH. The largest difference between the NH and SH is around 4.7% for TES^C. When the TDS-1 satellite collects data in the predetermined orbit, the geometry characteristics of data collected over the ocean of the NH and SH are different due to their different land and ocean distribution. This may be the reason for the different sea ice sensing results in the NH and SH.

Compared with other methods, the strategy of TEWS^D method is easy to understand and implement. It simply transforms the three-dimensional DDM to two-dimensional delay waveforms, which benefits a lot for computing. The nature of

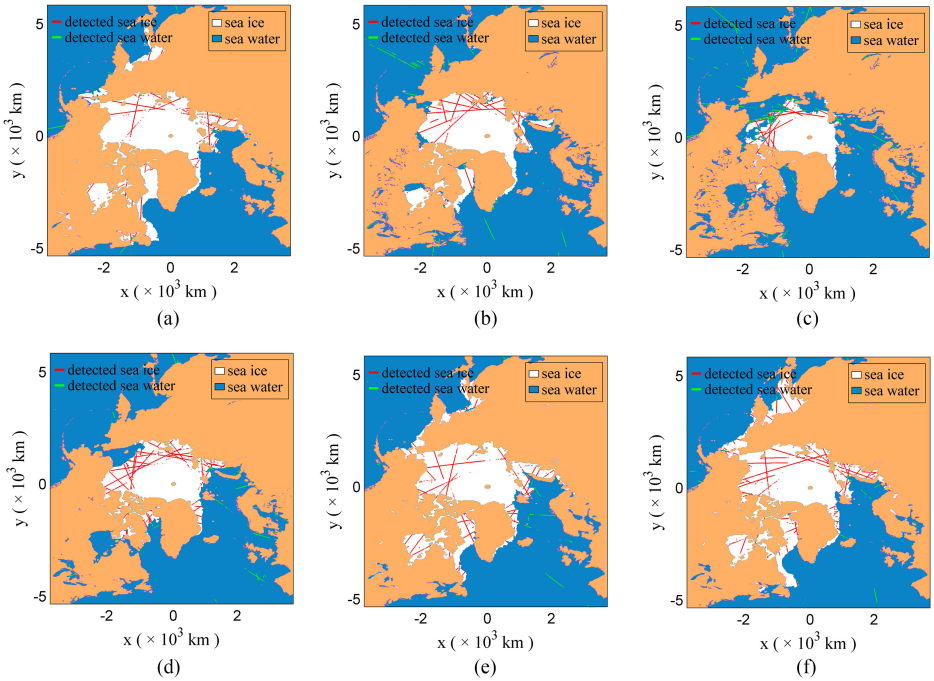

Fig. 9. GNSS-R sea ice detection results compared with the OSISAF SIE map of six different days for the Northern Hemisphere. (a) 28.02.2015. (b) 05.06.2015. (c) 08.08.2015. (d) 03.11.2015. (e) 14.01.2016. (f) 02.03.2016.

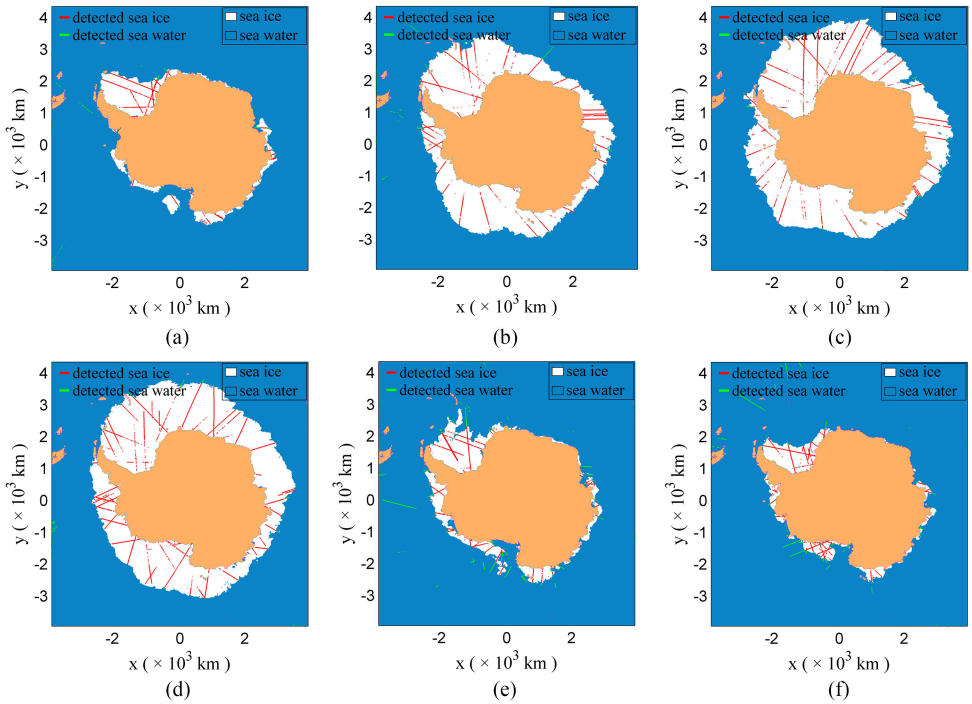

Fig. 10. GNSS-R sea ice detection results compared with the OSISAF SIE map of six different days for the Southern Hemisphere. (a) 28.02.2015. (b) 05.06.2015. (c) 08.08.2015. (d) 03.11.2015. (e) 14.01.2016. (f) 02.03.2016.

high efficiency can promote its application in real-time data processing.

Sea ice can be classified into first-year ice and multiyear ice according to the stage of development that is related to age. The first-year ice is sea ice of no more than one year's growth developing from young ice and disappears in the next melting season, while multiyear ice is sea ice that has survived at least one melt season. First-year and multiyear ice have different properties, which could affect the characteristics of reflected GNSS signals. Therefore, it is necessary to analyze the impact of SIT on sea ice sensing.

According to the results presented above, the performance of the TEWS^D estimator is more satisfactory than that of others. Therefore, the performance of first-year and multiyear ice for the

TEWS^D decision variables is computed. The OSISAF SIT data are used as the ground truth in this analysis and the PDF of first-year and multiyear ice for the TEWS_7^D estimator is shown in Fig. 8. The POF of first-year ice is 1.44%, while that of multiyear ice is 1.69%. It means the probability of successful detection of first-year ice is a little better than that of multiyear ice. The possible reason is that the surface of first-year ice is smoother than that of multiyear ice.

C. GNSS-R Data Tracks Compared With OSISAF SIE Map

The sea ice sensing results obtained from the GNSS-R data using the TEWS approach together with the SIE data from OSISAF for six different days of the NH and SH are presented in Figs. 9 and 10, respectively. The time span of the results shown is almost one year from 28 February 2015 to 2 March 2016. Note that the sea ice extent in the NH decreases from February 2015 to August 2015 and then increases from August 2015 to March 2016, while the situation is reversed for the SH. The presence of sea ice is marked by red line, whereas the presence of sea water is marked by the green line, which is compared with the sea ice (white) and water (blue) extent from the OSISAF. There are some gaps in the GNSS-R tracks since some DDMs of low quality are excluded during the data preprocessing steps. In total, about 38.2% of the data are discarded. In the data processing, we found that low-quality DDMs usually appear continuously for a period of time. Therefore, the gaps are often large with a distance greater than 50 km and the amount of low-quality DDMs from sea water surface is higher than that of sea ice. Moreover, the low-quality DDM also appears individually sometimes, which results in a very small gap.

The reflection over sea ice is usually coherent, while that over sea water is often diffusive and incoherent. Therefore, the SNR of scattered signals over sea ice is usually stronger than that of sea water. In general, the condition of sea ice is more stable, whereas the sea water surface can be easily affected by ocean winds, which often changes with time. Another factor related to data quality is the geometry characteristics, such as the incidence angle. This may be the reason for the consecutive appearance of low-quality DDMs.

V. Conclusion

This article has presented a method to sense sea ice presence over the NH and SH based on Doppler spread analysis using data from the TDS-1 mission. The two-dimensional delay waveforms derived from DDM are used as basic observables to depict the characteristics of reflected surface. Through analyzing the Doppler spread characteristics, three delay waveforms termed as CDW, IDW, and DDW are introduced and used for extracting GNSS-R observables. First, a data filter scheme is proposed based on the SD and RMSE of the first 48 delay bins of DDW. Then, different decision variables based on the TES and TEWS are used in this article for sensing sea ice. The use of TEWS of DDW achieves the best performance for distinguishing sea ice from water. Through validating with the OSISAF SIE data, the TEWS^D obtained a probability of successful detection of 98.22% and 96.65% for the NH and SH, respectively. Finally, the effect of SITs on sensing sea ice has been analyzed. Unfortunately, the relation between reflected signals and SITs has not been obtained in this article.

Acknowledgment

The authors would like to thank the EUMETSAT OSISAF for providing SIE and SIT product. They would also like to thank Surry Satellite Technology Ltd. (SSTL) and the Measurement of Earth Reflected Radio-navigation Signals By Satellite (MERRBYS) for providing the TDS-1 data.

Many thanks to the editors and three anonymous reviewers for their professional and valuable comments.

References

[1] G. A. Meehl, J. M. Arblaster, C. M. Bitz, C. T. Chung, and H. Teng, "Antarctic sea-ice expansion between 2000 and 2014 driven by tropical Pacific decadal climate variability," *Nat. Geosci.*, vol. 9, pp. 590–595, 2016.

[2] W. N. Meier *et al.*, "Arctic sea ice in transformation: A review of recent observed changes and impacts on biology and human activity," *Rev. Geophys.*, vol. 52, pp. 185–217, 2014.

[3] W. Dierking and T. Busche, "Sea ice monitoring by L-band SAR: An assessment based on literature and comparisons of JERS-1 and ERS-1 imagery," *IEEE Trans. Geosci. Remote Sens.*, vol. 44, no. 4, pp. 957–970, Apr. 2006.

[4] C. Hall and R. Cordey, "Multistatic scatterometry," in *Proc. IEEE Int. Geosci. Remote Sens. Symp., Remote Sens. Moving Toward 21st Century*, 1988, pp. 561–562.

[5] M. Martin-Neira, "A passive reflectometry and interferometry system (PARIS): Application to ocean altimetry," *ESA J.*, vol. 17, pp. 331–355, 1993.

[6] V. U. Zavorotny, S. Gleason, E. Cardellach, and A. Camps, "Tutorial on remote sensing using GNSS bistatic radar of opportunity," *IEEE Geosci. Remote Sens. Mag.*, vol. 2, no. 4, pp. 8–45, Dec. 2014.

[7] G. Foti *et al.*, "Spaceborne GNSS reflectometry for ocean winds: First results from the UK TechDemoSat-1 mission," *Geophys. Res. Lett.*, vol. 42, pp. 5435–5441, 2015.

[8] W. Li *et al.*, "Initial results of typhoon wind speed observation using coastal GNSS-R of BeiDou GEO satellite," *IEEE J. Sel. Topics Appl. Earth Observ. Remote Sens.*, vol. 9, no. 10, pp. 4720–4729, Oct. 2016.

[9] A. Santamaría-Gómez and C. Watson, "Remote leveling of tide gauges using GNSS reflectometry: Case study at Spring Bay, Australia," *GPS Solutions*, vol. 21, pp. 451–459, 2017.

[10] Q. Yan and W. Huang, "Tsunami detection and parameter estimation from GNSS-R delay-Doppler map," *IEEE J. Sel. Topics Appl. Earth Observ. Remote Sens.*, vol. 9, no. 10, pp. 4650–4659, Oct. 2016.

[11] K. Yu, "Weak tsunami detection using GNSS-R-based sea surface height measurement," *IEEE Trans. Geosci. Remote Sens.*, vol. 54, no. 3, pp. 1363–1375, Mar. 2016.

[12] A. Di Simone, H. Park, D. Riccio, and A. Camps, "Sea target detection using spaceborne GNSS-R delay-Doppler maps: Theory and experimental proof of concept using TDS-1 data," *IEEE J. Sel. Topics Appl. Earth Observ. Remote Sens.*, vol. 10, no. 9, pp. 4237–4255, Sep. 2017.

[13] J. Mashburn, P. Axelrad, S. T. Lowe, and K. M. Larson, "Global ocean altimetry with GNSS reflections from TechDemoSat-1," *IEEE Trans. Geosci. Remote Sens.*, vol. 56, no. 7, pp. 4088–4097, Jul. 2018.

[14] C. Chew and E. Small, "Soil moisture sensing using spaceborne GNSS reflections: Comparison of CYGNSS reflectivity to SMAP soil moisture," *Geophys. Res. Lett.*, vol. 45, pp. 4049–4057, 2018.

[15] A. Camps *et al.*, "Sensitivity of GNSS-R spaceborne observations to soil moisture and vegetation," *IEEE J. Sel. Topics Appl. Earth Observ. Remote Sens.*, vol. 9, no. 10, pp. 4730–4742, Oct. 2016.

[16] S. Vey, A. Güntner, J. Wickert, T. Blume, H. Thoss, and M. Ramatschi, "Monitoring snow depth by GNSS reflectometry in built-up areas: A case study for Wettzell, Germany," *IEEE J. Sel. Topics Appl. Earth Observ. Remote Sens.*, vol. 9, no. 10, pp. 4809–4816, Oct. 2016.

[17] A. Komjathy, J. Maslanik, V. U. Zavorotny, P. Axelrad, and S. J. Katzberg, "Sea ice remote sensing using surface reflected GPS signals," in *Proc. IEEE Int. Geosci. Remote Sens. Symp., Taking Pulse Planet, Role Remote Sens. Manag. Environ. (Cat. No. 00CH37120)*, 2000, pp. 2855–2857.

[18] M. Wiehl and B. Legrésy, "Potential of reflected GNSS signals for ice sheet remote sensing," *Prog. Electromagn. Res.*, vol. 40, pp. 177–205, 2003.
[19] M. B. Rivas, J. A. Maslanik, and P. Axelrad, "Bistatic scattering of GPS signals off Arctic sea ice," *IEEE Trans. Geosci. Remote Sens.*, vol. 48, no. 3, pp. 1548–1553, Mar. 2010.
[20] S. Gleason, "Remote sensing of ocean, ice and land surfaces using bistatically scanner GNSS signals from low earth orbit," Ph.D. dissertation, Univ. Surrey, Guildford, U.K., 2006.
[21] S. Gleason, "Towards sea ice remote sensing with space detected GPS signals: Demonstration of technical feasibility and initial consistency check using low resolution sea ice information," *Remote Sens.*, vol. 2, pp. 2017–2039, 2010.
[22] F. Fabra *et al.*, "Phase altimetry with dual polarization GNSS-R over sea ice," *IEEE Trans. Geosci. Remote Sens.*, vol. 50, no. 6, pp. 2112–2121, Jun. 2012.
[23] J. Strandberg, T. Hobiger, and R. Haas, "Coastal sea ice detection using ground-based GNSS-R," *IEEE Geosci. Remote Sens. Lett.*, vol. 14, no. 9, pp. 1552–1556, Sep. 2017.
[24] Z. Yun *et al.*, "Detection of Bohai Bay sea ice using GPS-reflected signals," *IEEE J. Sel. Topics Appl. Earth Observ. Remote Sens.*, vol. 8, no. 1, pp. 39–46, Jan. 2015.
[25] P. Jales and M. Unwin, "Mission description-GNSS reflectometry on TDS-1 with the SGR-ReSI," Surrey Satellite Technol. Ltd., Guildford, U.K., Tech. Rep. SSTL Rep. 248367, 2015.
[26] A. Rius, E. Cardellach, F. Fabra, W. Li, S. Ribó, and M. Hernández-Pajares, "Feasibility of GNSS-R ice sheet altimetry in Greenland using TDS-1," *Remote Sens.*, vol. 9, no. 7, p. 742, 2017.
[27] W. Li, E. Cardellach, F. Fabra, A. Rius, S. Ribó, and M. Martín-Neira, "First spaceborne phase altimetry over sea ice using TechDemoSat-1 GNSS-R signals," *Geophys. Res. Lett.*, vol. 44, pp. 8369–8376, 2017.
[28] C. Hu, C. Benson, C. Rizos, and L. Qiao, "Single-pass sub-meter space-based GNSS-R ice altimetry: Results from TDS-1," *IEEE J. Sel. Topics Appl. Earth Observ. Remote Sens.*, vol. 10, no. 8, pp. 3782–3788, Aug. 2017.
[29] Q. Yan and W. Huang, "Spaceborne GNSS-R sea ice detection using delay-Doppler maps: First results from the UK TechDemoSat-1 mission," *IEEE J. Sel. Topics Appl. Earth Observ. Remote Sens.*, vol. 9, no. 10, pp. 4795–4801, Oct. 2016.
[30] Q. Yan, W. Huang, and C. Moloney, "Neural networks based sea ice detection and concentration retrieval from GNSS-R delay-Doppler maps," *IEEE J. Sel. Topics Appl. Earth Observ. Remote Sens.*, vol. 10, no. 8, pp. 3789–3798, Aug. 2017.
[31] Q. Yan and W. Huang, "Sea ice sensing from GNSS-R data using convolutional neural networks," *IEEE Geosci. Remote Sens. Lett.*, vol. 15, no. 10, pp. 1510–1514, Oct. 2018.
[32] A. Alonso-Arroyo, V. U. Zavorotny, and A. Camps, "Sea ice detection using UK TDS-1 GNSS-R data," *IEEE Trans. Geosci. Remote Sens.*, vol. 55, no. 9, pp. 4989–5001, Sep. 2017.
[33] Y. Zhu, K. Yu, J. Zou, and J. Wickert, "Sea ice detection based on differential delay-Doppler maps from UK TechDemoSat-1," *Sensors*, vol. 17, p. 1614, 2017.
[34] V. U. Zavorotny and A. G. Voronovich, "Scattering of GPS signals from the ocean with wind remote sensing application," *IEEE Trans. Geosci. Remote Sens.*, vol. 38, no. 2, pp. 951–964, Mar. 2000.
[35] P. M. Woodward, "Radar ambiguity analysis," Royal Radar Establishment, Malvern, U.K., Tech. Note 731, 1967.
[36] J. Tye, P. Jales, M. Unwin, and C. Underwood, "The first application of stare processing to retrieve mean square slope using the SGR-ReSI GNSS-R experiment on TDS-1," *IEEE J. Sel. Topics Appl. Earth Observ. Remote Sens.*, vol. 9, no. 10, pp. 4669–4677, Oct. 2016.
[37] M. P. Clarizia, C. S. Ruf, P. Jales, and C. Gommenginger, "Spaceborne GNSS-R minimum variance wind speed estimator," *IEEE Trans. Geosci. Remote Sens.*, vol. 52, no. 11, pp. 6829–6843, Nov. 2014.
[38] L.-A. Breivik, S. Eastwood, and T. Lavergne, "Use of C-band scatterometer for sea ice edge identification," *IEEE Trans. Geosci. Remote Sens.*, vol. 50, no. 7, pp. 2669–2677, Jul. 2012.
[39] S. Aaboe *et al.*, "Ocean & sea ice SAF: Sea ice products user's manual, OSI-402-c, OSI-403-c," *Meteo France, Ifremer, EUMETSAT, DMI*, Norwegian Meteorol. Inst. Darmstadt, Germany, Tech. Rep. 205, 2018.
[40] L.-A. Breivik, S. Eastwood, Ø. Godøy, H. Schyberg, S. Andersen, and R. Tonboe, "Sea ice products for EUMETSAT satellite application facility," *Can. J. Remote Sens.*, vol. 27, pp. 403–410, 2001. [Online]. Available: http://osisaf.met.no/docs

Yongchao Zhu was born in Hubei, China. He received the B.S. and M.S. degrees in geomatics engineering and the Ph.D. degree in geodesy and geomatics engineering from Wuhan University, Wuhan, China, in 2012, 2014, and 2018, respectively.

He was a Visiting Ph.D. Student with German Research Center for Geosciences GFZ for 18 months, i.e., from January 2017 to July 2018. He is currently with the College of Civil Engineering, Hefei University of Technology, China. His research interests include ocean and land remote sensing applications using GNSS-reflectometry techniques.

Tingye Tao was born in Anhui, China. He received the B.S. degree in geomatics engineering from Wuhan University, Wuhan, China, in 2001, the M.S. degree in geomatics from Hefei University of Technology, Hefei, China, in 2005, and the Ph.D. degree in geodesy and geomatics engineering from Wuhan University, in 2010. He is currently with the Hefei University of Technology. His research interests include deformation monitoring technology and GNSS-reflectometry techniques.

Kegen Yu (Senior Member, IEEE) received the Ph.D. degree in electrical engineering from the University of Sydney, Sydney, NSW, Australia, in 2003.

He was with the Jiangxi Geological and Mineral Bureau, Nanchang University, Nanchang, China; University of Oulu, Oulu, Finland; CSIRO ICT Centre, Marsfield, NSW, Australia; Macquarie University, Sydney, NSW, Australia; University of New South Wales, Sydney, NSW; and Wuhan University, Wuhan, China. He is currently with the School of Environmental Science and Spatial Informatics, China University of Mining and Technology, Xuzhou, China. His current research interests include Global Navigation Satellite Systems (GNSS) reflectometry and ground-based and satellite-based positioning

Zhenxuan Li received the Ph.D. degree from the China University of Mining and Technology, Xuzhou, China, in 2018.

He is currently a Lecturer with the College of Civil Engineering, Hefei University of Technology, Hefei, China. His research interests include very high resolution remote sensing image processing, information extraction, and change detection.

Xiaochuan Qu received the Ph.D. degree in geodesy and geomatics engineering from Wuhan University, Wuhan, China, in 2014.

He is currently a Lecturer with the College of civil engineering, Hefei University of Technology, Hefei, China. His current research interests include GNSS Meteorology, tropospheric, and ionospheric delay modeling.

Zhourun Ye was born in Anhui, China. He received the B.S. degree in geomatics engineering from Liaoning Technical University, Liaoning, China, in 2007 and the M.S. and Ph.D. degrees in geodesy and geomatics engineering from the University of Chinese Academy of Sciences, Beijing, China in 2010 and 2015, respectively.

He was a Visiting Ph.D. Student with the University of Stuttgart, Stuttgart, Germany, for 24 months, i.e., from November 2012 to October 2014.

Jun Geng received the M.S. degree from Nanjing Forestry University, Nanjing, China, in 2012, and the Ph.D. degree from Nanjing University, Nanjing, China, in 2016.

He is currently a Lecturer with the School of Civil Engineering, Hefei University of Technology, Hefei, China. His research interests include quantitative remote sensing of vegetation and its applications for ecosystem.

Jingui Zou was born in Hubei, China. He received the B.S. degree in engineering surveying from the Wuhan Technical University of Survey and Mapping, Wuhan, China, and the Ph.D. degree in geodesy and geomatics engineering from Wuhan University, Wuhan, China, in 1996 and 2002, respectively.

He is currently a Professor with the School of Geodesy and Geomatics, Wuhan University. His research interests include GNSS-R, and multisensor integration and applications.

Maximilian Semmling received the graduate degree in physics from Leipzig University, Leipzig, Germany, in 2007 and the Ph.D. degree from Technical University Berlin, Berlin, Germany, in 2012.

Since 2008, he has been with Department for Geodesy, German Research Centre for Geosciences (GFZ), Potsdam, Germany. His research interests include GNSS and remote sensing techniques with focus on GNSS reflectometry.

Jens Wickert received the Graduate degree in physics from the Technical University Dresden, Dresden, Germany, in 1989, and the Ph.D. degree in geophysics/meteorology from the Karl-Franzens-University Graz, Austria, in 2002.

He is the Research Topic Director "The atmosphere in global change" with the German Research Center for Geosciences (GFZ), Potsdam, Germany, and the Responsible Scientist for GNSS remote sensing research. In addition, he holds a professorship for "GNSS Remote Sensing, Navigation and Positioning" with the Technische Universität Berlin, Berlin, Germany. He is the Principle Investigator of several national and international research projects, including GNSS-related satellite experiments and missions.